ELSEVIER

Journal of Volcanology and Geothermal Research 120 (2002) 25–42

Journal of volcanology and geothermal research

www.elsevier.com/locate/jvolgeores

Flow and fracture maps for basaltic rock deformation at high temperatures

Valentina Rocchi [a,*], Peter R. Sammonds [a], Christopher R.J. Kilburn [b]

[a] *Mineral, Ice and Rock Physics Laboratory, Department of Geological Sciences, Gower Street, University College London, London, UK*

[b] *Benfield Greig Hazard Research Centre, Department of Geological Sciences, Gower Street, University College London, London, UK*

Received 14 February 2002; received in revised form 20 March 2002; accepted 20 March 2002

Abstract

Understanding how the strength of basaltic rock varies with the *extrinsic* conditions of stress state, pressure and temperature, and the *intrinsic* rock physical properties is fundamental to understanding the dynamics of volcanic systems. In particular it is essential to understand how rock strength at high temperatures is limited by fracture. We have collated and analysed laboratory data for basaltic rocks from over 500 rock deformation experiments and plotted these on principal stress failure maps. We have fitted an empirical flow law (Norton's law) and a theoretical fracture criterion to these data. The principal stress failure map is a graphical representation of ductile and brittle experimental data together with flow and fracture envelopes under varying strain rate, temperature and pressure. We have used these maps to re-interpret the ductile–brittle transition in basaltic rocks at high temperatures and show, conceptually, how these failure maps can be applied to volcanic systems, using lava flows as an example.

Keywords: creep; fracture; flow; principal stress maps; basalt; diabase

1. Introduction

Pervasive fracturing of rock at high temperatures is a dominant feature of volcanic systems: whether this is fracturing of the country rock surrounding magma chambers (inferred from seismic activity; Newhall and Punongbayan, 1996), or fracturing of lava domes (Fink and Griffiths, 1998), fracturing of the crust of mobile lava flows (Fig. 1), or their solidifying fronts (Kilburn, 1993, 2000). As a result, understanding how the strength of rock varies with the specific *extrinsic conditions* of stress state, pressure and temperature, and the *intrinsic conditions* of composition and water content, joints, flaw and crack damage, crystal and vesicle size, content and anisotropy is fundamental to understanding the dynamics of volcanic systems. Two diverse examples are the conditions for magma ascent and the emplacement of lava flows. Thus, magma ascent is affected by many independent factors such as the tectonic setting and pressure changes within the magma. However, it is the failure of the host

* Corresponding author. Tel.: +44-20-7679-7378.
E-mail addresses: ucfbvro@ucl.ac.uk (V. Rocchi), p.sammonds@ucl.ac.uk (P.R. Sammonds), c.kilburn@ucl.ac.uk (C.R.J. Kilburn).

0377-0273/02/$ – see front matter
PII: S0377-0273(02)00343-8

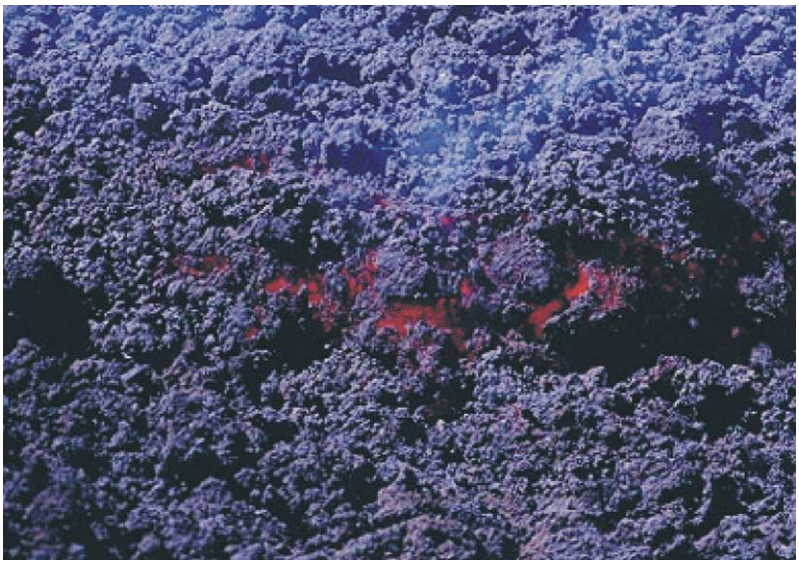

Fig. 1. Photograph of a typical aa flow surface. The carapace of the flow continuously fractures forming a surface rubble.

rock below the volcanic edifice, involving fracture at elevated temperatures, that leads to the opening of new pathways through which fresh magma is able to reach the surface (Gudmundsson, 1998, 1995; Ryan, 1994; Shaw, 1980). The second example, lava flows, involves the primary hazard from effusive volcanoes, and modelling rates of flow advance and maximum potential length are important goals for hazard mitigation (Kilburn, 1996, 2000). Again, many factors affect the way a flow evolves, including effusion rate, cooling processes, channel pressures and the topography of the ground over which it travels. It has long been recognised that material properties, such as rheology are important controls on lava behaviour (Nichols, 1939), but only recently has the importance of lava *strength* also been addressed (Kilburn, 1996).

Indeed, fracture in general plays a crucial role in limiting material strength (Griffith, 1921). To understand how rock strength at high temperatures varies with extrinsic and intrinsic conditions it is essential to understand how these affect both flow and fracture, and how flow 'strength' is limited by fracture. Sometimes this is counter-intuitive. We advocate that *principal stress failure maps*, introduced by Hallam and Ashby (1990) and employed for instance by Sammonds et al. (1998) to describe sea ice fracture, are the best means of representing rock flow and fracture and interpreting for ductile–brittle transition, under conditions of stress, pressure and temperature relevant to volcanic systems.

In this paper, we introduce the use of principal stress failure maps and discuss their application to investigating the deformation of predominantly basic igneous rocks. The principal stress failure map is a graphical representation of ductile and brittle experimental data together with mechanical models of flow and fracture plotted in two dimensions on maximum and minimum principal stress axes, σ_1 and σ_3, shown in schematic form in Fig. 2. (We use the convention that the principal stresses are denoted by $\sigma_1 \geq \sigma_2 \geq \sigma_3$; tension positive.) When $\sigma_1 = \sigma_2 = \sigma_3 = P$, the rock is subject only to hydrostatic pressure, P, and the axis of symmetry on the map, $\sigma_3 = \sigma_1$ is called the hydrostat. The map has a tension–tension quadrant where simple and biaxial tensile test data are plotted, a compression–compression quadrant, and two tension–compression quadrants where data from confined extension tests are plotted. For the conventional triaxial deformation test, which is the most common rock mechanics test, two of the applied stresses have equal values, $\sigma_1 = \sigma_2 > \sigma_3$, (they are referred to as the confining pressure,

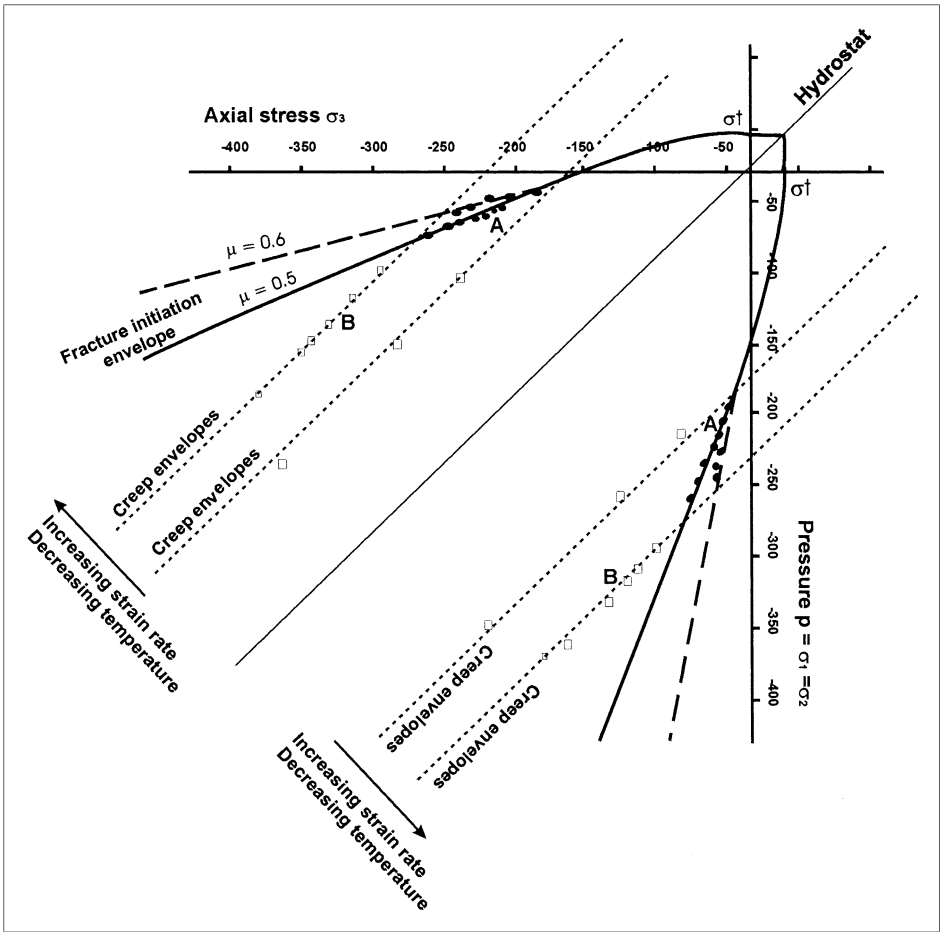

Fig. 2. Principal stress map showing creep, fracture initiation criterion. The influence of temperature, strain rate and friction coefficients are shown. The tensile strength σ_t and the compressive strength σ_c are shown. At high temperatures or low strain rates the rock will deform in a ductile manner. Creep data (squares) will lie on creep envelopes representing the flow power law. If the specimen is deformed at high strain rates and low pressures (full circles labelled A), the specimen will fail a brittle manner by shear fracture. The increase of strength with pressure is mapped by the nonlinearity of the failure envelope. At high pressures (labelled B) the specimen will deform by rate-dependent plastic creep without fractures initiating from flaws.

p) and results are plotted in the compression–compression quadrant on the map for axial stress, σ_3, against confining pressure, $P = \sigma_1$. Ductile deformation results fall on *creep envelopes* for a particular creep strain rate, which are parallel to the hydrostat. The *fracture envelope* truncates the creep envelopes as fracture limits strength. (A fuller description of the principal stress failure map is given below.)

Models and data for rock failure are also commonly plotted on two other representations: the *Mohr construction* and the *deformation mechanism map* (Frost and Ashby, 1982; Murrell, 1990). The Mohr construction plots shear stress against normal stress, but is poor at representing strain rate dependent processes. The deformation mechanism map plots shear stress against temperature, but is poor at representing the effect of normal stress (or pressure). The principal stress failure map can be employed to demonstrate both the effects of pressure and strain rate dependent processes. Therefore it is the best means of representing ductile flow, which is strongly dependent on strain rate, and the role of fracture in limiting strength, as

Table 1
Experimental data of volcanic rocks used to construct in the principal stress maps

Rock type	Test type	Notes on lithology	Diff. strength (MPa)	Strain rate (s−1)	Confining pressure (MPa)	Temp. (°C)	Reference	Ref. No.	Notes
Cuerbio Basalt	TC	Porphyritic; 80% olv; 17% pyx; 4% feld. Porosity 5–8%	60–225	1.0 E-4	0–50	20–945	Bauer et al. (1981)	1	FRACTURE
Cuerbio Basalt	TC	Porphyritic; 80% olv; 17% pyx; 4% feld. Porosity 5–8%	5–550	1.0 E-4	0–50	20–1000	Friedman et al. (1979)	2	FRACTURE
Knippa Basalt	UC	N.A.	262	N.A.	30	20	Bredthauer (1957)	3	FRACTURE
Dresser Basalt	UC	N.A.	329	5.0 E-5	0	20	Rohde and Feng (1990)	4	FRACTURE
Dresser Basalt	TC	Fine-grained 500 μm crystals; some pyx phenocrysts throughout	7–1385	1.9 E-4 to 2.4 E-1	0–689	573–1656	Lindholm et al. (1974)	5	FRACTURE
Basalt Breccia	TC	Brecciated and altered	34–190	5.0 E-5	0.1–700	23	Carmichael (1989)	6	FRACTURE
Hanford Basalts	T	Fine-grained theolitic flood basalt	11–26	N.A.	0	20	Schultz (1993,1995)	7,8	FRACTURE
Hanford Basalts	UC	Fine-grained theolitic flood basalt	81–479	N.A.	0	20	Schultz (1993,1995)	7,8	FRACTURE
Azizya Basalt	TC	Massive; no fractures. Density 2.89 g/cm^3	94	2.1 E-5	0	20	Mahmoud (1980)	9	FRACTURE
Azizya Basalt	T	Massive; no fractures. Density 2.89 g/cm^3	19	2.1 E-5	0	20	Mahmoud (1980)	9	FRACTURE
French Massif Central basalt	UC	*Pheno*: homogeneous mixture plag; olv; pyx; opaques average size 250 μm. *Gm*: glassy	50–340	2.2 E-6	0	20–1000	Duclos and Paquet (1991)	10	FRACTURE
Basic rocks including diabase and basalt	TC	N.A	150–2000	N.A.	0–545	20	Lockner (1995)	11	FRACTURE. Data extrapolated
Hyogo Basalt	C	*Pheno*: 20–25% olv; *Glm*: 50% plag; 15–20% clinopyx; 5% rhombic pyx	2–24	3.7 E-10 to 7.2 E-12	0	20	Iida et al. (1960)	12	DUCTILE. Creep rate at 50 h
Uvalde Basalt	UC	Massive; homogeneous; no fractures; in decreasing order: olv; aug; hornb; qtz; plag; biot	57–450	N.A.	0	25	Overton and Moczygemba (1967)	13	FRACTURE
Panamint Valley Basalt	C	*Glm*: fine 92%; *Pheno*: 1% olv; 1% clinpyx; 3% orthopyx; 3% plag	170–2480	1.2 E-4 to 1.4 E-7	990–1050	675–875	Hacker and Christie (1991)	14	DUCTILE with 0.5 wt% H_2O
Basalt	TC	Very fine-grained; 66% plag; 8% olv; 26% iron minerals	186–406	1.0 E-6 to 2.0 E3	0	25	Kumar (1968)	15	FRACTURE. Data extrapolated
Basalt	TC	N.A.	151–1650	4.3 E-4	200–500	25–800	Griggs et al. (1960)	16	FRACTURE. Data extrapolated
Basalt	TC	N.A.	260–1540	1 E-4	500	25–800	Handin and Carter (1979). Original data in Handin (1966)	17	FRACTURE
Mount Hood Andesite	TC	Fine-grained; matrix contains small amounts of glass.	5–225	1.5 E-4	0–50	600–920	Bauer et al. (1981)	1	DUCTILE and FRACTURE
Mount Hood Andesite	TC	N.A.	70–220	1.0 E-4 to 1.0 E-7	0–50	25	Carmichael (1989)	6	FRACTURE

Table 1 (*Continued*).

Rock type	Test type	Notes on lithology	Diff. strength (MPa)	Strain rate (s−1)	Confining pressure (MPa)	Temp. (°C)	Reference	Ref. No.	Notes
Mount Hood Andesite	TC	*40% Pheno* (*avrg. size 5 mm*): 30% plag; 5% pyx; 1% hornb; 1% olv; 1% magn. *60% Gm* (*avrg. size* $<$*1 mm*): feld; magn; glass. Porosity: 10–12%	75–305	1.5 E-4 to 1.5 E-7	0–50	20–1000	Friedman et al. (1979)	2	FRACTURE
Andesite	TC	N.A.	0–150	N.A.	0–150	20	Lockner (1995)	11	FRACTURE. Data extrapolated
Japanese Andesite	C	*Pheno*: 5–10% plag; 5–10% chlo. *Gm*: 50% plag; 2% clinopyx; 30% chlo	8–22	2.4 E-10 to 2.4 E-11	0	27	Iida et al. (1960)	12	DUCTILE. Creep rate at 50 h
Kumacho Andesite	TC	Porosity: 5.6%	133–180	0	0	25	Inada and Yokota (1984)	18	Dry and wet conditions
Kumacho Andesite	T	Porosity: 5.6%	12	N.A.	0	25	Inada and Yokota (1984)	18	Dry and wet conditions
Palisades Diabase	UC	N.A.	241	0	0	25	Schultz (1995)	8	FRACTURE
Frederick Diabase	UC	N.A.	487	0	0	25	Schultz (1995)	8	FRACTURE
Casacta and Chapadao diabase	UC	N.A.	152–228	N.A.	0	25	Schultz (1995)	8	FRACTURE
Palisades Diabase	T	N.A.	11.4	0	0	25	Schultz (1995)	8	FRACTURE. Point load test
Frederick Diabase	T	N.A.	40	N.A	0	25	Schultz (1995)	8	FRACTURE. Direct tension test
Columbia Diabase	C	70 plag; 23% pyx; 3% chlo; 3% magn. Grain size: 200 μm	400	1.2 E-5 to 8.2 E-7	400–450	940–1040	Mackwell et al. (1998)	19	DUCTILE
Maryland Diabase	C	56% plag; 38% pyx; 5% pige; 1% magn. Grain size 50–300 μm	450	3.12 E-07	450	970	Mackwell et al. (1998)	19	DUCTILE
Maryland Diabase	TC	36% plag; 58% clinopyx; 3% chlo; 3% opaque minerals	500	4.50 E-06	500–1500	600–900	Carmichael (1989)	6	FRACTURE/ DUCTILE
Maryland Diabase	HD	58% clinopyx; 36% plag; 3% opaques; 3% chlo. Average size 75 μm	530	4.50 E-06	530	600	Kronenberg and Shelton (1980)	20	FRACTURE. Data extrapolated

Key: C, creep; T, tension; TC, triaxial compression; UC, uniaxial compression. Abbreviations of minerals: biot, biotite; chlo, chlorite; feld, feldspar; hornb, hornblende; magn, magnetite; olv, olivine; pige, pigeonite; plag, plagioclase; pyx, pyroxene.

fracture is strongly dependent on normal stress or pressure.

To construct principal stress failure maps specific experimental data are needed. After a comprehensive literature review of numerous deformation experiments on basaltic rocks over a wide range of test conditions we have constructed the failure maps which we present below, and then used them to re-interpret the experimental data and the ductile–brittle transition. Basaltic lava forms and evolves from fluid to solid state, under limited temperature and pressure conditions: between about 1200 and 500°C and from atmospheric pressure to about 3–4 MPa. In the case of magma host rock, temperatures may range from 1200°C to as low as 100–200°C, but pressures may reach 75 MPa, corresponding to about 3-km depth in the crust. However few laboratory deformation experiments have been done on basaltic rocks under conditions of high temperature and comparatively low pressure: only a handful of fracture experiments have been done under these conditions (see below). We have therefore constructed failure maps for conditions relevant to volcanic systems by extrapolation from experimental data gathered over a wide range of conditions, but point out where further experimental research is required to validate these extrapolations. We then show, conceptually, how these failure maps can be applied to volcanic systems, using lava flows as an example. (A complete solution requires a detailed stress analysis, which is beyond the scope of this paper.)

2. High-temperature mechanical tests on basic igneous rocks

The rheology of molten lava, besides temperature, is strongly controlled by silica content, water content, crystal content, polymerisation, vesiculation and degassing (for a review, see Dragoni, 1993). Kilburn (1993) pointed out that as molten lava cools, in the crystallisation interval (nominally from 1200 to 950°C for basalts) compressive strength increases from 0 to $\sim 10^8$ Pa, thereafter remaining at about 10^8 Pa during cooling to room temperature (Murrell and Chakravarty, 1973) and the inferred tensile strength increases from 0 to $\sim 10^7$ Pa. These changes brought about by cooling of the molten lava to a sub-solidus rock exhibiting considerable strength have significant effects on the dynamics of volcanic systems. Nevertheless, the influence of both the *extrinsic* conditions of stress state, pressure and temperature and the *intrinsic* rock properties on strength have only been investigated to a limited degree, particularly under the conditions prevailing in volcanic systems. Our interest is principally in basaltic volcanism, but as Mackwell et al. (1998) commented, there have been remarkably few experimental studies on the mechanical behaviour of basaltic rocks. Even if intrusive rocks of basaltic composition are included this picture does not change much. They attribute this paucity, in part, to the difficulty in locating sample material suitable for mechanical testing with the required grain size distributions. Most basalts contain too much glassy component to provide realistic flow laws and most lower crustal gabbros have grain sizes that are too large to meet the requirements of mechanical test apparatus.

We have collected all published data for the flow and fracture of basic igneous rocks tested under a range of conditions using different testing techniques. In Table 1 are listed the rock types surveyed in this paper: the data set contains 554 experimental test results taken from 20 papers on more than 20 igneous rock types and represents the most comprehensive survey undertaken. Intrusive igneous rocks such as diabase (dolerite) well represent volcanic rocks in experimental studies due to the appropriate grain size distribution, low glass content and mineralogical composition (Mackwell et al., 1998). We have also included test data from andesites. Andesites are in the same broad isomechanical group as basalts (see discussion below and Murrell, 1990). Clearly, it is a matter of interest to interrogate how significant changing to a more acidic composition is compared to the gross change in the physical process in transition from flow to fracture. All data are plotted on the principal stress failure map in Fig. 3. On the principal stress maps in Figs. 4–7 subsets of the data are plotted.

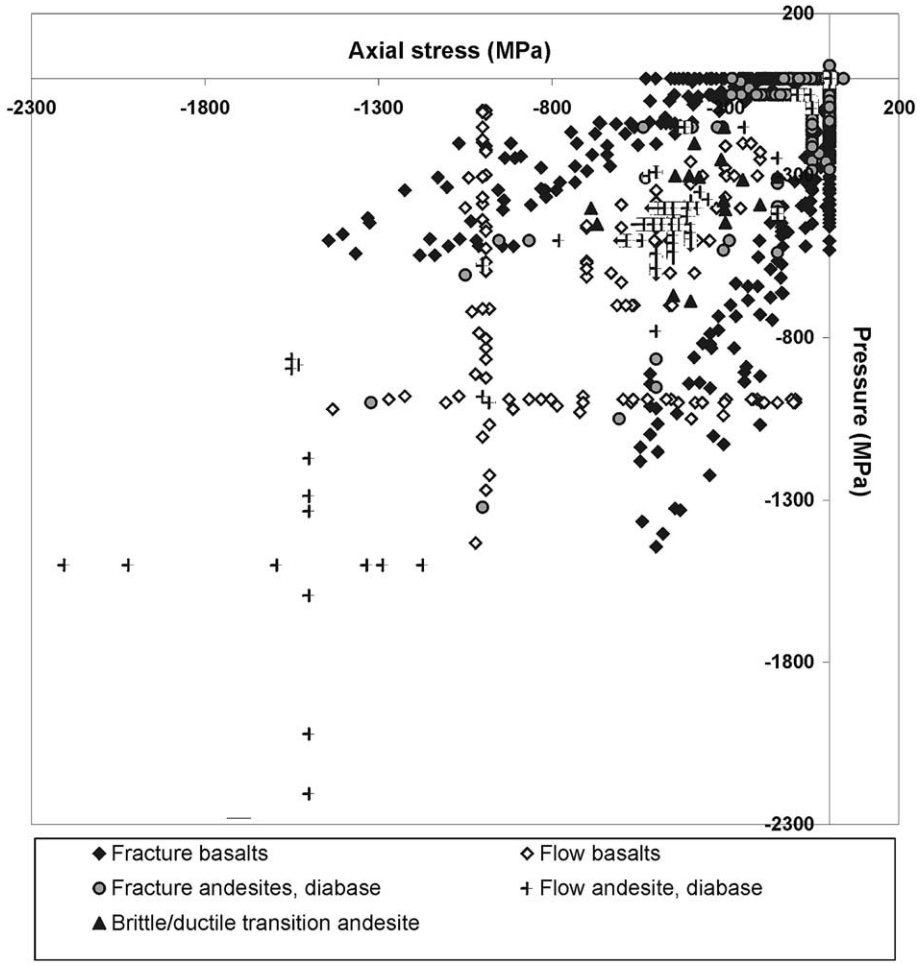

Fig. 3. Principal stress map showing the entire range of data collected. Data comes from basalts, andesites and diabase and covers all temperature and pressure ranges. This diagram shows the large amount of basalt data available at high pressures. (Data from all references listed in Table 1.)

Early high-temperature mechanical experiments on basic igneous rocks were creep (constant load) tests done under unconfined conditions (i.e. atmospheric pressure) in torsion (Lomnitz, 1956), bending (Iida et al., 1960) and uniaxial compression (Murrell and Chakravarty, 1973). Later research has been directed at high confining pressures of 400 MPa or more (see Carter, 1976 for a review of early work; Carter and Kirby, 1978; Hacker and Christie, 1991; Mackwell et al., 1998). However, there have been a number of studies under the conditions of high temperatures and low pressures of volcanic systems. Lindholm et al. (1974) did strength (controlled strain rate tests) and dynamic tests on basalt under a broad range of conditions, including a few at low pressures. Friedman et al. (1979) studied the strength and ductility of basalts in strength tests at low pressures and temperatures up to partial melting. But most high-temperature data come from experiments done at pressures between 250 and 1500 MPa, and predominately at the highest pressures.

These experiments show that the creep strain of rock at high temperature at time t can be described empirically by the sum of instantaneous elastic and plastic strain during loading ($\varepsilon_e+\varepsilon_p$), the transient creep strain (ε_t), the steady-state

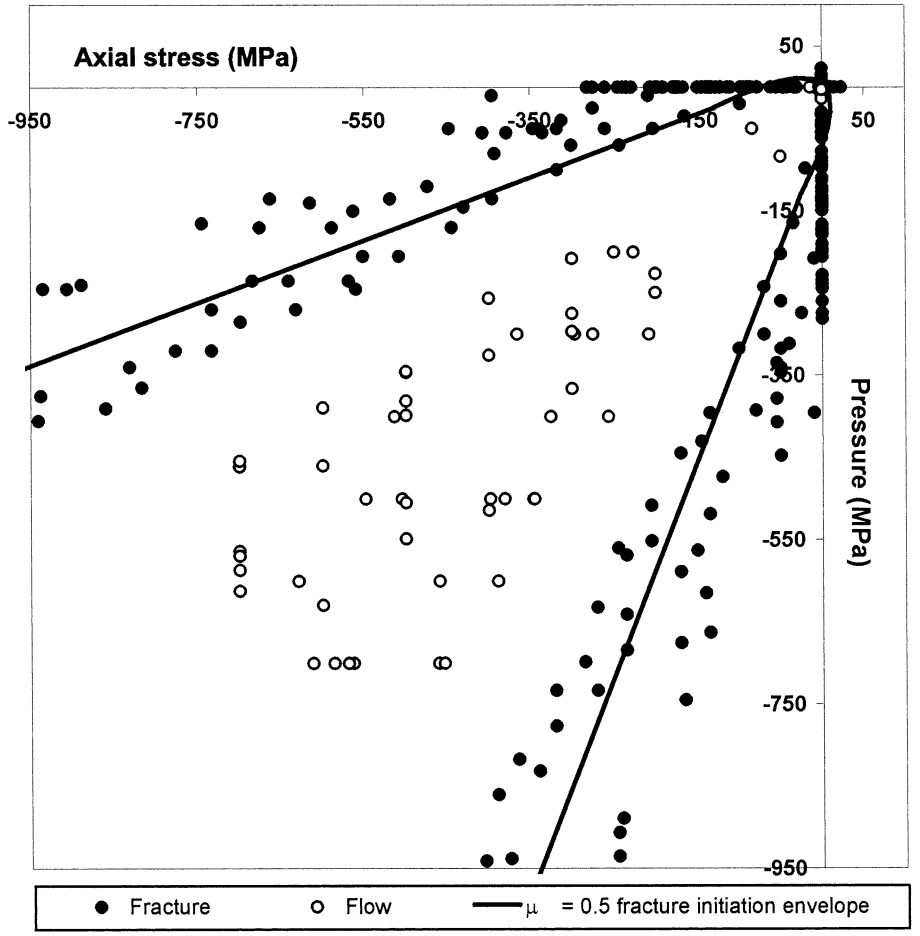

Fig. 4. Principal stress diagram showing only basalt-room temperature data and the fracture criterion for closed cracks with a friction coefficient equal to $\mu = 0.5$. This model shows how the fracture criterion almost perfectly delineates the data (Data from references 1–4, 6–13, 15–17 listed in Table 1).

creep strain (ε_{ss} t) and the accelerating creep strain (ε_a) (Carter, 1976):

$$\varepsilon(t) = (\varepsilon_e + \varepsilon_p) + \varepsilon_t(t) + \varepsilon_{ss}t + \varepsilon_a \quad (1)$$

The creep strain represents the sum of competing rate-dependent deformation mechanisms with their own dependence on temperature, pressure and strain history (Frost and Ashby, 1982). High-temperature transient creep is best represented by (Carter and Kirby, 1978):

$$\varepsilon_t = \varepsilon_{\text{total}}[1-\exp(-t/t_R)] \quad (2)$$

where t_R is the relaxation time. Steady-state flow is described by the power law creep equation (Frost and Ashby, 1982):

$$\dot{\varepsilon} = A_o\sigma_s^n \exp-(Q/RT) \quad (3)$$

where σ_s is the effective shear stress and ε_s is the effective strain rate (see Appendix); T is the temperature in Kelvin; R is the molar gas constant; Q is the activation energy for creep; and n is the power law exponent. A_o is a pre-exponential scalar constant (involving the crystal lattice atomic vibration frequency) that would contain a factor dependent on developing lava fabric. In general steady-state flow observed in these experiments is well described by the creep power law.

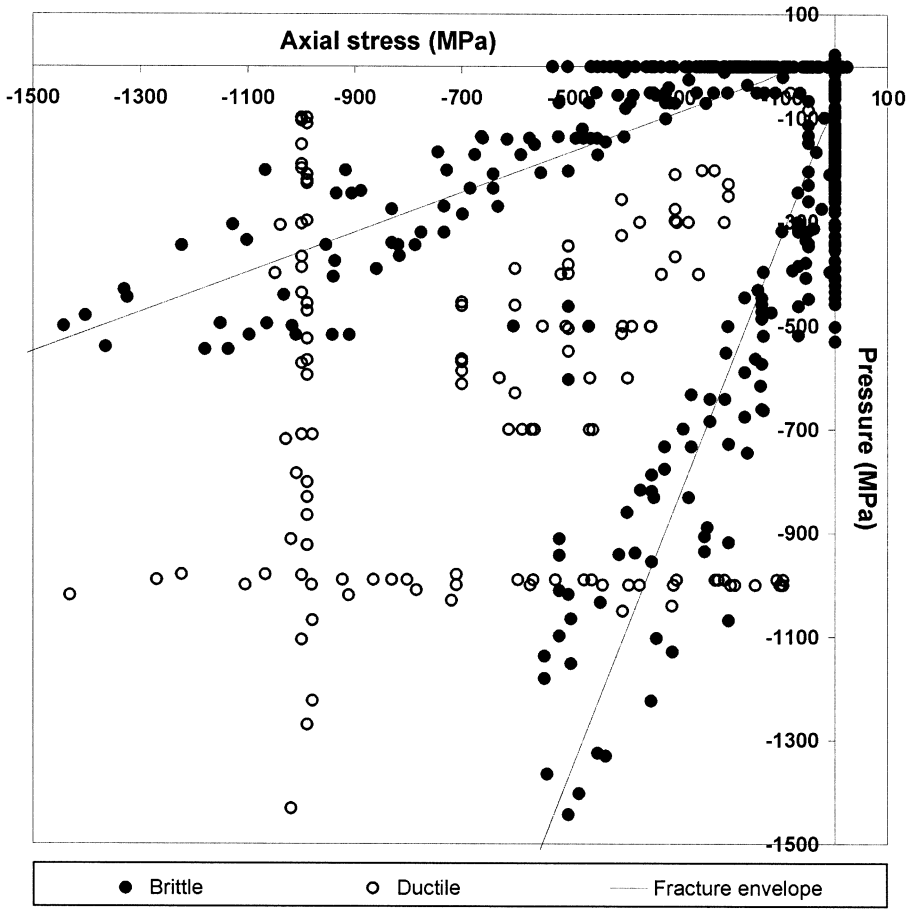

Fig. 5. Principal stress diagram showing only basalt data at all temperatures. The same fracture criterion for closed cracks with a friction coefficient equal to $\mu = 0.5$ was used as for the room temperature data. This accordance of the same fracture envelope with high temperature data and room temperature data shows how the brittle fracture criterion is independent of temperature. (Data from references 1–17 listed in Table 1).

The fracture data are less well modelled. Lindholm et al. (1974) employed a fracture criterion with an activation energy for fracture. However, as we argue below, flow and fracture are competing mechanisms, best represented on a principal stress failure map. Creep-brittle processes are poorly modelled. Handin and Carter (1979) commented that, whereas our understanding of the flow of rocks under very high pressure is good, we have much to learn about creep in the semi-brittle state under relatively low confining pressures. This situation is little changed.

A number of the experimental studies have addressed themselves to how intrinsic rock properties affect the deformation of basalts. Basaltic rocks vary systematically in their phase proportions and composition with changes in pressure and temperature and consequently so do their mechanical properties (Hacker and Christie, 1991). Deformation experiments have been done on the main constituents of rocks of basaltic composition: plagioclase (e.g. Borg and Heard, 1969; Marshall and MacLaren, 1977; Tullis and Yund, 1987) and pyroxene (e.g. Ave Lallement, 1978; Kolle and Blacic, 1982; Kirby and Kronenberg, 1984). Tullis et al. (1991) have proposed that basalts can be modelled as a two-component mixture, where the parameters in the power law creep

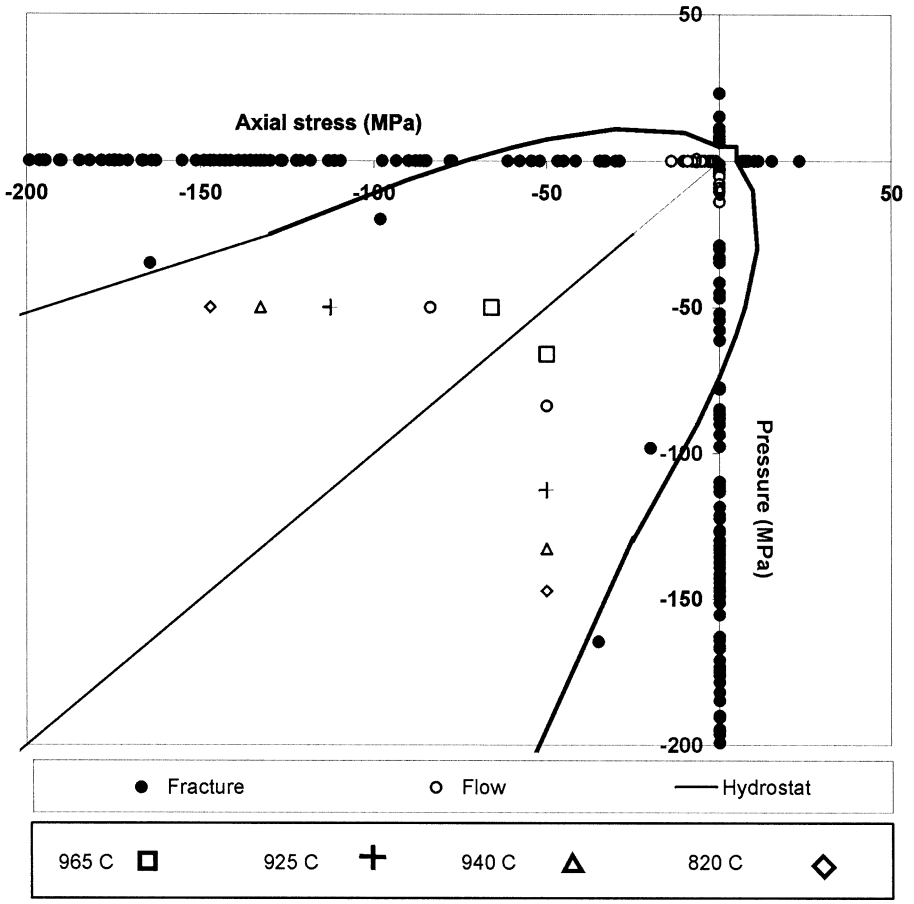

Fig. 6. Principal stress diagram for brittle and ductile basalt data at low pressures and all temperatures. This diagram shows how data coming from experiments under these conditions is very scarce (Data from references 1, 2, 5, 7, 8, 10–13, 16 listed in Table 1).

equation are weighted by the fractional composition:

$$n_a = 10^{(f_1 \log n_1 + f_2 \log n_2} \tag{4}$$

$$Q_a = \frac{Q_2(n_a - n_1) - Q_1(n_a - n_2)}{(n_2 - n_1)} \tag{5}$$

$$A_a = 10^{\frac{\log A_2(n_a - n_1) - \log A_1(n_a - n_2)}{n_2 - n_1}} \tag{6}$$

The subscripts are for components *1* and *2*, and the aggregate, *a*. *f* is the volume fraction.

The results of Mackwell et al. (1998), who tested diabase with two different plagioclase contents, do seem to conform to this: increasing fractional content of plagioclase significantly increased the creep rate. Hacker and Christie (1991) have examined the influence of glass content. They found that at higher temperatures, above 800°C, their test samples were notable weak as the glass became mobile and flow into cracks. The glass content could be modelled by:

$$\sigma_{\text{glassy}} = \sigma_{\text{crystalline}}(1 - \lambda \phi^{2/3}) \tag{7}$$

where ϕ is the glassy volume fraction and λ is an empirical constant. Hydrolytic weakening has an important role to play. Mackwell et al. (1998) found that their dry diabase rocks were approx-

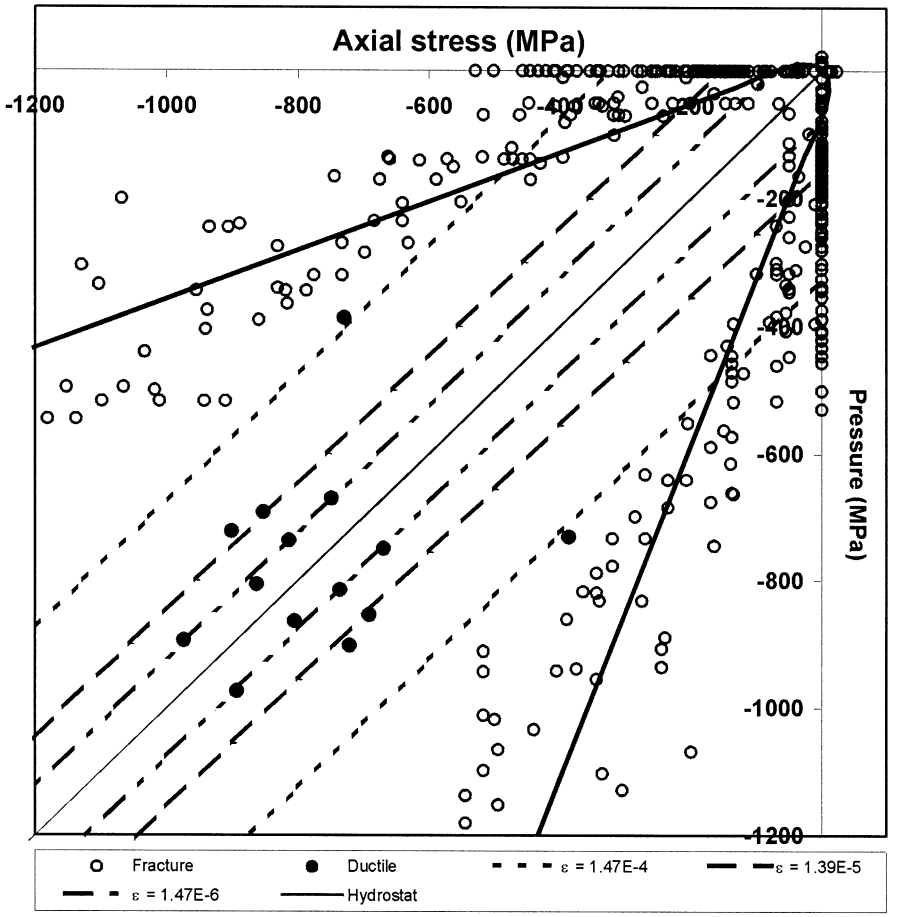

Fig. 7. Principal stress diagram for ductile and brittle data, together with fracture and creep envelopes. Creep envelopes at four strain rate values were constructed using coefficients calculated with linear regression fit. Ductile data has been normalised to a temperature value of 875°C (Data from references 1–17 in Table 1).

imately 1.6 times stronger than 'as received' or wet rocks of the same type and under similar conditions. The strength of the dry rock has significant implications for the tectonics of Venus as compared with Earth. The role of water is complex, however, we note that Hirth and Kohlstedt (1996), when modelling the lithosphere, accounted for hydrolytic weakening by modifying the activation energy for creep.

There has been little similar work on the effect of intrinsic physical properties on the creep-brittle and fracture behaviour of basaltic rocks. Microcracks can form during creep deformation owing to localised tensile stresses and locally high fluid pressures, as observed by Murrell and Chakravarty (1973). This has been modelled in materials engineering by Shapery (1986), but not applied to creep-brittle behaviour of basalt. Porosity has a strong effect on fracture as measured by the material's fracture toughness. Theoretically, fracture toughness has been shown by Rice (1977) to decrease nonlinearly with porosity:

$$K_\phi = K_0 e^{-m\phi} \tag{8}$$

where K_0 is the fracture toughness at zero porosity and m is a constant dependent on pore shape and distribution. Experiments on porous ice conform to this relation (Rist et al., 1999) but its applicability to basalts is untested. Water has

been shown to have a strong influence on weakening dolerite through stress corrosion cracking (Meredith and Atkinson, 1983). Schultz (1995) has examined how jointing weakens basaltic rock masses. However, our approach is not to treat jointing as a material property but as a structural process (Balme et al., 2002).

3. Principal stress maps of flow and fracture

The principal stress failure map (Fig. 2) can be used to plot results from creep and fracture tests of creep-brittle materials obtained from laboratory deformation experiments (Hallam and Ashby, 1990). Fully dense flow is driven by the shear stress alone and is independent of pressure, or mean stress, except at very high pressures of the Earth's mantle (Frost and Ashby, 1982). Steady-state isotropic flow can be described by the power law creep equation. On the principal stress map, the flow stress for power law creep at a particular creep strain rate is represented by lines, or *envelopes*, which are parallel to the $\sigma_3 = \sigma_1$ hydrostat, as flow stress is independent of pressure (although there may be an enhancement of the creep rate with confining pressure due to the effects of dynamic recrystallisation (Derby, 1990). The effect of decreasing temperature is that the creep envelopes move outward from the hydrostat as the rock becomes more creep resistant. Microcracks and vesicular content will have the effect of enhancing the creep rate, which will result in the creep envelopes moving closer to the hydrostat as the rock becomes weaker, and will also introduce a small pressure dependency. However, such effects are small compared to the overall more important factors such as stress and temperature.

Griffith (1924) showed that fracture initiation occurs in brittle solids once the local tensile stress at the tip of the most favourably oriented pre-existing crack exceeds the uncracked material's tensile strength, σ_T. Fracture initiation criteria have been obtained by the theoretical treatment of ellipsoidal cracks in an arbitrary triaxial stress field by Murrell and Digby (1970), which are given in full in Appendix. For open cracks the fracture initiates when a function of the remotely applied principal stresses, σ_1 and σ_3, causes the local crack-tip tensile stress to equal σ_T:

$$f(\sigma_1, \sigma_3, \nu) = \sigma_T \tag{9}$$

where ν is Poisson's ratio. On the principal stress map this is a parabolic fracture envelope, symmetric about the hydrostat. When normal stresses across open cracks exceed about ten times the tensile strength, $10\ \sigma_T$, the cracks will close (Digby and Murrell, 1976) and a different closed crack fracture initiation criterion has to be used:

$$f(\sigma_1, \sigma_3, \nu, \mu) = \sigma_T \tag{10}$$

where μ is the coefficient of friction, acting to oppose sliding on the crack faces. On the principal stress map this is a linear envelope in the compression–compression quadrant. These fracture initiation criteria are strongly dependent on pressure or normal stress, but are independent of temperature.

It should be noted that the closed crack fracture initiation criterion is Coulombic in form, $|\tau| - \mu\ \sigma_n = \text{constant}$, where τ and σ_n are the shear and normal stresses, respectively, hence the linear envelope. These criteria can also be re-caste in terms of the fracture mechanics parameter, the fracture toughness, instead of σ_T. It should also be noted that in triaxial compression, fracture does not lead directly to failure. For rock there is strong evidence that many cracks propagate stably under increasing stress before interacting to form a shear fault (e.g. Sammonds et al., 1992). This would result in a fracture envelope that truncates the creep envelopes at higher stresses (Hallam and Ashby, 1990). However, the process of crack linkage and shear fault formation still remains to be adequately modelled.

The stress path during a typical triaxial deformation, constant strain rate or 'strength' test, can be followed on the principal stress map. Typically, a test starts at zero stress (at the origin), and a confining pressure, p, is first applied, so that the stress path initially follows the hydrostat. Once the test confining pressure is achieved, the axial stress σ_3 is increased and deformation will be elastic until the creep envelope corresponding to the

applied strain rate is reached. This envelope marks the boundary of elastic behaviour, and hence, the term 'creep envelope'. However, for stress states outside the fracture initiation envelope fracture will initiate; for stress states inside the envelope, the rock will deform by power-law creep. The point of intersection of the fracture initiation envelope with the $\sigma_3 = 0$ principal stress axis represents the *tensile strength* and the intersection with the $\sigma_1 = p = 0$ the *uniaxial compressive strength*.

4. Experimental data and their representations

We have constructed the creep envelopes using the power-law creep equation (Eq. 3) with data from laboratory triaxial deformation tests on basaltic rocks only. The peak differential stresses required for ductile deformation attained during constant strain rate 'strength' tests have been shown to be the same as the stresses required to induce minimum strain rates in constant stress 'creep' tests (Mellor and Cole, 1982). Ductile strength data can therefore be expected to conform to the power-law creep equation and hence lie on the creep envelopes of the principal stress map at that creep strain rate. As all the tests are in axisymmetric loading, the shear strain rate and equivalent shear stress are:

$$\overline{\varepsilon} = \sqrt{3}/2\dot{\varepsilon}_3\overline{\sigma}_s = \sigma_3/\sqrt{3} \qquad (11)$$

We normalised the power law with the temperature of crystallisation before analysing the data. The stress exponent n, the activation energy Q and the lattice constant A were determined with a linear regression fit of all basaltic data points of creep experiments.

In Figs. 4–8 we focussed only on basaltic rocks, and in Fig. 6 only on pressures and temperatures more relevant to volcanic conditions, showing how most of the data lie outside these limits when comparing to Figs. 4 and 5. We plotted all the collected basaltic rock data only onto principal stress maps at different temperatures and strain rates to establish under what temperature or strain rate conditions the data best fit the models. In Fig. 4 we plot a principal stress map for all room temperature fracture data using the closed crack fracture initiation criterion with $\mu = 0.5$ to show how they almost exactly delineate the fracture envelope. We have constructed all fracture initiation envelopes using the tensile strength values for Hanford basalt, equivalent to 11 MPa (Schultz, 1995). The validity of the closed-crack triaxial failure model is seen also when plotting data up to 1350°C where all rocks that fractured in a brittle manner lie almost entirely along the fracture initiation envelope (Fig. 5). Using data in all temperature ranges and at pressures up to 200 MPa, which corresponds to a depth of 8 km, the data set was very poor indicating the lack of data necessary for the understanding of volcanological problems (Fig. 6). This leaves only one low-pressure ductile deformation data point inside the failure envelope, and only two fracture data points on the brittle fracture envelope, except for uniaxial compression tests which lie along the axis. Four additional fracture data points lie inside the fracture envelope. These points however, correspond to tests performed at temperatures above 820°C on a basaltic rock on which temperature had a strong weakening effect. This plot shows also that the data points tend to the fracture envelope as temperature is decreased and when plotting only data at temperatures and pressures appropriate for volcano conditions, very few data points are available. Power law creep envelopes were constructed using the coefficients obtained by linear least square regression fit on all stress-strain rate data at each temperature for basaltic samples. The power law coefficients were found to be different for two temperature ranges: up to and above 775°C. The power law coefficients that best fit the low temperature range data are: $n = 5.5 \pm 0.5$, $A = 1.27 \pm 0.4 \times 10^{-9}$ $(\mathrm{MPa})^{-5.5} s^{-1}$, $Q = 291 \pm 37$ kJ mol^{-1}; and $n = 3.2 \pm 0.8$, $A = 4.38 \pm 10 \times 10^{-3}$ $(\mathrm{MPa})^{-3.2} s^{-1}$, $Q = 209 \pm 138$ kJ mol^{-1}, for high-temperature range data. Two principal stress diagrams were plotted using this flow law, one showing strain rate dependent creep envelopes, where the temperature was kept constant at 875°C (Fig. 7), and one showing temperature dependent creep envelopes, keeping strain rate constant at 1.47×10^{-6} s^{-1} (Fig. 8).

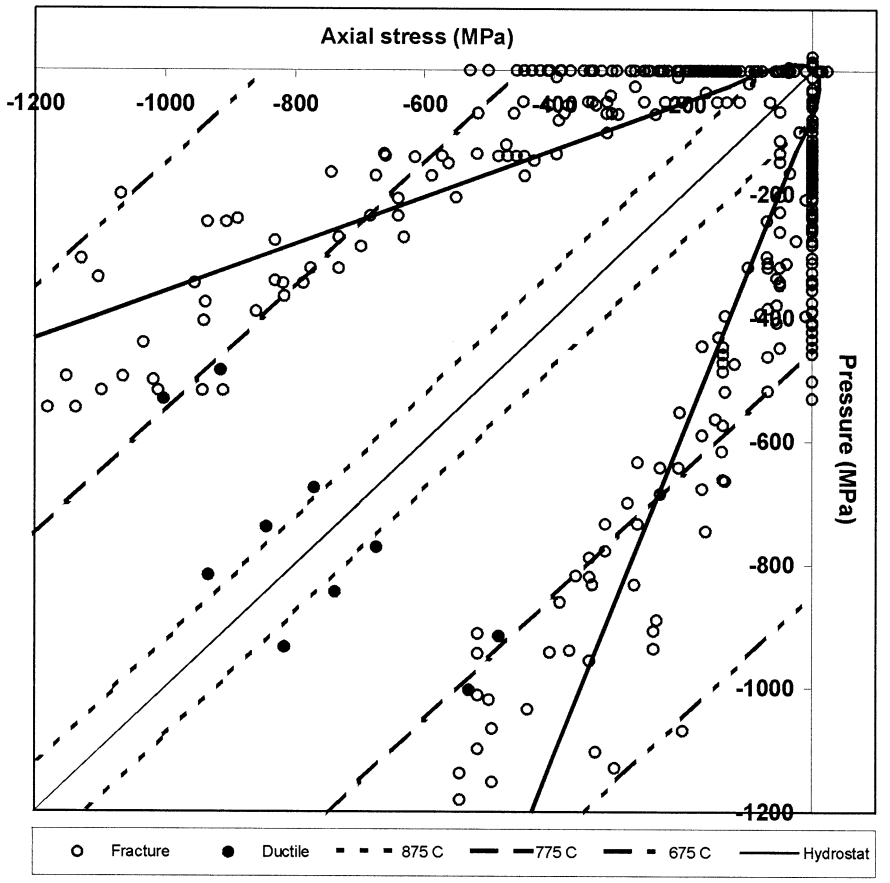

Fig. 8. Principal stress diagram for ductile and brittle data, together with fracture and creep envelopes. Creep envelopes at four temperature values were constructed using coefficients calculated with linear regression fit. Ductile data has been normalised to strain rate value of 1.47×10^{-6} (Data from references 1–17 in Table 1).

5. Discussion

The principal stress maps shown above were constructed using experimental data from at least 20 different volcanic rock types, including mainly basalts but also diabase and andesite. Fracture models, power-law creep models and the failure data plotted on the maps belong to different rock types and used different test conditions. Nevertheless all data conform to the same fracture criterion and all equal rock types conform to the same creep power law. The fracture criterion predicts well the stresses at which failure occurs regardless of temperature, proving the opposite of the common thought that rock failure is a temperature-dependent phenomenon. This can be seen by comparing two principal stress maps: for experiments done at all temperatures up to 1350°C (Fig. 5), and for room temperature experiments (Fig. 4). All brittle fracture data lie on or outside the fracture envelope and all flow data are enclosed within the creep envelope. The data points for brittle deformation, which lie inside the fracture envelope, correspond either to high-temperature data or data produced with very low strain rate experiments. Therefore, principal stress maps represent well the failure criterion for most basic rocks under widely varying conditions and show how data broadly fit models of flow and fracture.

For modelling purposes, however, if the failure

criterion and the power law creep model are to be used for predicting what stresses and temperatures a rock will fail and under what regime, compression tests and fracture toughness or tension tests (for the failure envelope construction) should be performed for the same rock type at a range of temperatures and pressures. Data plotted on the diagrams show obvious gaps in the data set at certain confining pressures and especially at low differential stresses (Fig. 6). Lines of data seen, in particular in Fig. 5, come from series of experiments done at a constantly high confining pressure, but different strain rates or temperatures. This demonstrates that there is a concentration of data in certain areas and that the data set needs to be widened to a broader range of pressures. It is well known how rock behaves under compression–compression quadrant (quadrant 3) as well as in the simple tension (quadrant 1), however there is no data in the tension–compression quadrant (quadrants 2 and 4). Further experiments need to be done under these stress conditions, as these are particularly important for the stress conditions applicable to advancing lava flows.

Principal stress maps may also be used for a post-analysis of data and to infer specific rock properties. The closed-crack triaxial failure criterion (Eq. A6) produces different failure envelopes according to what friction coefficient value is used. By fitting the fracture envelope to the fracture data, one could estimate the value for the friction coefficient. Figs. 4–8 show the best fit between the failure envelope and the data tested at room temperature for a coefficient of friction of 0.5. This particular value was chosen after plotting the data and seeing where it spread in the axial stress-confining pressure space. This method could also prove useful in testing the validity of known values of friction coefficients.

The final observation concerns creep power laws. All deformation data were plotted onto two separate maps for flow laws at constant temperature (Fig. 7) and constant strain rate (Fig. 8). The differential stress obtained during constant strain rate tests has been shown to be the same as the stress required to induce a minimum strain rate in constant load creep tests. Therefore, ductile strength data can be expected to lie over the power law creep equation lines on the principal stress maps. Indeed some data points follow well the equation but not enough ductile strength experiments have been performed to further verify the model. As strain rates decreases, the creep envelopes move further from the hydrostat and often truncate the fracture envelope. A few data points for brittle to ductile transition were collected and indeed lie close to intersection point of the fracture initiation and the creep envelopes (Fig. 3). Similarly, as the temperature is lowered from 875°C to 675°C the creep lines open towards the brittle failure envelope intersecting the fracture envelope only at much higher stresses. Both phenomena are related to the micro-mechanism occurring when deforming the rock with constant load experiments at temperatures above 0.4 T_M. The micro-structural characteristic of this plastic behaviour is dislocation creep where the rock can deform in a plastic manner by the climb of dislocation from sources in the glide planes (Weertman, 1968), where rapid deformation and lower temperatures will inhibit ductile behaviour.

Finally, principal stress maps also provide a useful way of characterising areas where data is lacking and further experiments need to be performed as well as verifying the model and visualising in a rapid and simple way what type of failure may occur and under what stress, strain and temperature conditions. This method of representing data and rock behaviour under different conditions could also find a potential use in studying volcanic flows on other planets.

The effect of the characteristic composition, the vesicle shape and content, and the grain size distribution, on the mechanical behaviour of basaltic rocks is similar to that on other rock types and can be represented only in terms of principal stresses, strains and temperatures as shown on principal stress diagrams. At the same time, this paper, being a compilation of all basaltic rock mechanics experiments, shows that there is a lack of data in the high-temperature low-pressure regime and in the tensile stress region. We also demonstrate the use of principal stress maps as a mean of collating data and representing creep and brittle failure models onto just one 2-D map by plotting all collected data onto these diagrams.

This is particularly convenient in the specific case of a lava flow where at least two dynamic regimes are observed and where the interplay of several factors needs to be understood by isolating the single most influencing factors in the evolution of a flow.

6. Application to lava flow

Lava flows are subject to a number of characteristic forces such as gravity and the resistance of the solidifying crust and strengthening lava crust and interior. The combination of such forces causes the rock to deform by both viscous flow and brittle fracture. Understanding the influence of tensile and shear stress, strain and temperature on each dynamic regime and how these factors interrelate with each other is a key to understanding how far a flow will advance and by what mechanisms. Principal stress failure maps are potentially an ideal tool for summarising and visualising the interactions between the governing factors.

7. Conclusions

The deformation mechanisms and the deformation properties of several intrusive and extrusive igneous rock types, all of which have been studied by laboratory experiments, have been collected and plotted on the same 2-D principal stress maps. The power law creep equation and the fracture criterion were also plotted on the same map to show where the transition from ductile to brittle behaviour occurs within this stress space.

Analysis of the maps shows that key data are missing for conditions appropriate for volcanic systems (e.g. temperatures up to 1100°C and pressures up to 50 MPa). Further experiments need to be performed on volcanic rocks especially at temperatures above 800°C.

Principal stress maps can become a useful tool in volcanology both for visualising the complex interplay between the stress, strain rate and temperature in an advancing lava flow, as well as for modelling purposes. This 2-D space on which we can contemporaneously represent experimental data, fracture envelopes for different friction coefficients, and creep envelopes for different strain rates and temperatures, offers the possibility of anticipating the modes of deformation for a range of conditions. Alternatively, a post-analysis combining failure criteria and experimental data allows us to further test the validity of the experimental data.

Acknowledgements

This research was supported through the European Union Framework V Environment Programme Contract No. ENV4-CT98-0713. Peter R. Sammonds is a Royal Society University Research Fellow. This paper has been improved by the helpful comments of Harry Pinkerton.

Appendix

Definitions of shear and fracture stresses

Ductile flow is driven by the shear stress alone and is independent of pressure, or mean stress so it is convenient to decompose the stress tensor, σ_{ij}, into its deviatoric and isotropic parts (see e.g. Ranalli, 1995):

$$\sigma_{ij} = s_{ij} + \overline{\sigma}\delta_{ij} \tag{A1}$$

where s_{ij} is the deviatoric stress tensor, $\overline{\sigma} = 1/3\sigma_{kk}$ is the mean stress and δ_{ij} is the Kronecker delta. Solid-state isotropic flow can be described by the power law creep equation:

$$\dot{\varepsilon}_s = A_o \sigma_s^n \exp -(Q/RT) \tag{A2}$$

$\dot{\varepsilon}_s$ is the effective strain rate, defined in terms of the strain rate tensor $\dot{\varepsilon}_{ij}$, or the principal strain rates, $\dot{\varepsilon}_I$ ($i = 1, 2, 3$):

$$\dot{\varepsilon}_s = (1/2\dot{\varepsilon}i_j\dot{\varepsilon}_{ij})^{1/2} = \sqrt{3}/2\sqrt{2}((\dot{\varepsilon}_1 - \dot{\varepsilon}_2)^2 + (\dot{\varepsilon}_2 - \dot{\varepsilon}_3) + (\dot{\varepsilon}_3 - \dot{\varepsilon}_1)^2)^{1/2} \tag{A3}$$

σ_s is the effective shear stress, which can be de-

fined in terms of the deviatoric stress tensor, s_{ij}, or principal stresses, σ_i ($i=1, 2, 3$):

$$\sigma_s = (1/2 s_{ij} s_{ij})^{1/2} = \sqrt{2}/2\sqrt{3}((\sigma_1-\sigma_2)^2+ (\sigma_2-\sigma_3)^2 + (\sigma_3-\sigma_1)^2)^{1/2} \quad \text{(A4)}$$

Murrell and Digby (1970) obtained the theoretical fracture initiation criterion for open ellipsoidal cracks in an arbitrary triaxial stress field (Eq. A5) and for cracks closed by high normal stresses (Eq. A6) where the criterion depends on the coefficient of friction, μ:

$$(\sigma_1-\sigma_3)^2-2(2-\nu)^2\sigma_T(\sigma_1+\sigma_3) = \nu(4-\nu)(2-\nu)^2\sigma_T^2 \quad \text{(A5)}$$

$$|\left(\sqrt{1+\mu}\right)-\mu|(\sigma_1-\sigma_3) = \alpha\sigma_T + 2\mu\sigma_3 \quad \text{(A6)}$$

where σ_T is the tensile strength, ν is Poisson's ratio, α is a numerical factor of about 3.5 for the biaxial case.

References

Ave Lallement, H.G., 1978. Experimental deformation of diopside and websterite. Tectonophysics 48, 1–27.

Balme, M.R., Rocchi, V., Sammonds, P.R. and Vita-Finzi, C., 2002. Experimental and Theoretical Fracture Mechanics Applied to Fracture of the Crust of Venus.

Bauer, S.J. Friedman, M. and Handin, J., 1981. Effects of water-saturated on strength and ductility of three igneous rocks at effective pressures to 50 MPa and temperatures to partial melting. In: Einstein, H.H, Scandriato, D.P. (Eds.), Rock Mechanics from Research to Application. Balkema, Rotterdam, pp. 79–84.

Borg, I.Y., Heard, H.C., 1969. Mechanical twinning in experimentally deformed plagioclase. Contrib. Mineral. Petrol. 23, 128–135.

Bredthauer, R.O., 1957. Strength characteristics of rock samples under hydrostatic pressure. Trans. Am. Soc. Mech. Eng., 122, 1049–1068.

Carmichael, R.S., 1989. Practical Handbook of Physical Properties of Rocks and Minerals. CRC Press, Boca Raton, FL.

Carter, N.L., Kirby, S.H., 1978. Transient creep and semibrittle behaviour of crystalline rocks. Pure Appl. Geophys. 116, 805–839.

Carter, N.L., 1976. Steady state flow of rocks. Rev. Geophys. 14, 301–360.

Digby, D.J., Murrell, S.A.F., 1976. The deformation of flat ellipsoidal cavities under large confining pressures. Bull. Seismol. Soc. Am. 66, 425–431.

Derby, B., 1990. Dynamic recrystallization and grain size. In: Barber, D.I., Meredith, P.G. (Eds.), Deformation Processes in Minerals, Ceramics and Rocks. Unwin Hyman, London, pp. 354–364.

Dragoni, M., 1993. Modelling the rheology and cooling of lava flows. In: Kilburn, C.R.J., Luongo, G. (Eds.), Active Lavas: Monitoring and Modelling. UCL Press, London, pp. 305–325.

Duclos, R., Paquet, J., 1991. High-temperature behaviour of basalts; role of temperature and strain rate on compressive strength and K_{Ic} toughness of partially glassy basalts at atmospheric pressure. Int. J. Rock Mech. Min. Sci. Geomech. Abs. 28 (1), 71–76.

Fink, J.H., Griffiths, R.W., 1998. Morphology, eruption rates, and rheology of lava domes: Insights from laboratory models. J. Geophys. Res. 103, 527–545.

Friedman, M., Handin, J.N., Higgs, G., Lantz, J.R., 1979. Strength and ductility of four dry igneous rocks at low pressures and temperatures to partial melting. Proc. Symp. Rock Mech. 35–50.

Frost, H.J. and Ashby, M.F., 1982. Deformation–Mechanism Maps. Pergamon, Oxford.

Griffith, A.A., 1921. The phenomena of rupture and flow in solids. Phil. Trans. R. Soc., London A221, 163–198.

Griffith, A.A., 1924. Theory of Rupture. Proc. First International Congress Applied Mechanics, Delft, pp. 55–63.

Griggs, D.T., Turner, F.J., Heard, H.C., 1960. Deformation of rocks at 500°C to 800°C. Geol. Soc. Am. Mem. 79, 39–104.

Gudmundsson, A., 1998. Magma chambers modelled as cavities explain the formation of rift zone central volcanoes and their eruption and intrusion statistics. J. Geophys. Res. 103, 7401–7412.

Gudmundsson, A., 1995. Infrastructure and mechanics of volcanic systems in Iceland. J. Volcanol. Geotherm. Res. 64 (1–2), 1–22.

Hacker, B.R., Christie, J.M., 1991. Experimental deformation of a glassy basalt. Tectonophysics 200 (1–3), 79–96.

Hallam, S.D., Ashby, M.F., 1990. Compressive brittle fracture and failure maps. In: Barber, D.J., Meredith, P.G. (Eds.), Deformation Processes in Minerals, Ceramics and Rocks. Unwin Hyman, London, pp. 84–108.

Handin, J., 1966. Strength and Ductility. Handbook of Physical Constants, Geo. Soc. Am. Mem. 97, pp. 223–289.

Handin, J., Carter, N., 1979. Rheological properties of rock at high temperatures. Proc. Congr. Int. Soc. Rock. Mech. 4 (3), pp. 97–106.

Hirth, G., Kohlstedt, D.L., 1996. Water in the Oceanic upper mantle: implications for the rheology melt extraction and the evolution of the lithosphere. Earth Planet. Sci. Lett. 144, 93–108.

Iida, K., Wada, T., Aida, Y., Shichi, R., 1960. Measurements of creep in igneous rocks. J. Earth Sci., Nagoya Univ. 8, 1–15.

Inada, Y., Yokota, K., 1984. Some studies of low temperature

rock strength. Int. J. Rock Mech. Min. Sci. Geomech. Abstr. 21 (3), 145–153.
Kilburn, C.R.J., 1993. Lava crusts, aa flow lengthening and the pahoehoe-aa transition. In: Kilburn, C.R.J., Luongo, G. (Eds.), Active Lavas: Monitoring and Modelling. UCL Press, London, pp. 263–280.
Kilburn, C.R.J., 1996. Patterns and predictability in emplacement of subaerial lava flows and flow fields. In: Scarpa, R., Tilling, R.I. (Eds.), Monitoring and Mitigation of Volcano Hazards. Springer, Berlin.
Kilburn, C.R.J., 2000. Lava flows and flow fields. In: Encyclopaedia of Volcanoes, Academic Press, San Diego, pp. 291–305.
Kirby, S.H., Kronenberg, A.K., 1984. Deformation of clinopyroxenite: evidence for a transition in flow mechanisms and semi-brittle behaviour. J. Geophys. Res. 89, 3177–3192.
Kolle, J.J., Blacic, J.D., 1982. Deformation of single crystal clinopyroxenes. J. Geophys. Res. 87, 4019–4034.
Kronenberg, A.K., Shelton, G.L., 1980. Deformation microstructures in experimentally deformed Maryland Diabase. J. Struct. Geol., 23, 341–352.
Kumar, A., 1968. The effects of stress rate and temperature on the strength of basalt and granite. Geophys. 33, 501–510.
Lindholm, U.S., Yeakley, L.M., Nagy, A., 1974. The dynamic strength and fracture properties of Dresser basalt. Int. J. Rock Mech. Min. Sci. Geomech. Abstr. 11, 181–191.
Lockner, D.A., 1995. Rock failure. In: Rock Physics and Phase Relations: Handbook of Physical Constants. AGU Ref., pp. 127–147.
Lomnitz, C., 1956. Creep measurements in igneous rocks. J. Geol. 25, 473–479.
Mackwell, S.J., Zimmerman, M.E., Kohlstedt, D.L., 1998. High-temperature deformation of dry Diabase with applications to tectonics on Venus. J. Geophys. Res., 103, 975–984.
Mahmoud, K.A., 1980. A study of the dynamic mechanical properties of rocks. J. Mines, Metals Fuels 128–132.
Marshall, D.B., MacLaren, A.C., 1977. Deformation mechanisms in experimentally deformed plagioclase feldspars. Phys. Chem. Miner. 1, 351–370.
Mellor, M., Cole, D.M., 1982. Deformation and failure of ice under constant stress and strain rate. Cold Reg. Sci. Technol. 5, 201–219.
Meredith, P.G., Atkinson, B.K., 1983. Stress corrosion and acoustic emission during tensile crack propagation in Whin Sill dolerite and other basic rocks. Geophys. J. R. Astron. Soc. 75, 1–21.
Murrell, S.A.F., Chakravarty, S., 1973. Some new rheological experiments on igneous rocks at temperatures up to 1120°C. Geophys. J. R. Astron. Soc. 34, 211–250.
Murrell, S.A.F., Digby, P.J., 1970. The theory of brittle fracture initiation under triaxial stress conditions; II. Geophys. J. R. Astron. Soc. 19, 499–512.
Murrell, S.A.F., 1990. Brittle-to-ductile transitions in polycrystalline non-metallic materials. In: Barber, D.J., Meredith, P.G. (Eds.), Deformation Processes in Minerals, Ceramics and Rocks. Unwin Hyman, London, pp. 109–137.
Newhall, C.G., Punongbayan, R.S. (Eds.), 1996. Fire and Mud: Eruptions and Lahars of Mount Pinatubo, Philippines. Philippine Institute of Volcanology and Seismology, Quezon City, and University of Washington Press, Seattle, pp. 285–305.
Nichols, R.L., 1939. Viscosity of lava. J. Geol. 47, 290–302.
Overton, H.L., Moczygemba, M., 1967. Some mechanical properties of homogeneous and heterogeneous basalt. The Log Analyst, May–July 22–28.
Ranalli, G., 1995. Rheology of the Earth. Chapman and Hall, London.
Rice, R.W., 1977. Microstructure dependence of mechanical behaviour. In: MacCroone, R.K. (Ed.), Properties and Microstructure: Treatise on Materials Science and Technology, vol. 11. Academic Press, San Diego, CA, pp. 20–369.
Rist, M.A., Sammonds, P.R., Murrell, S.A.F., Meredith, P.G., Doake, C.S.M., Oerter, H., Matsuki, K., 1999. Experimental and theoretical fracture mechanics applied to Antarctic ice fracture and surface crevassing. J. Geophys. Res. 104, 2973–2987.
Rohde, J., Feng, H., 1990. Analysis of the variability of unconfined compression tests of rocks. Rock Mech. Rock Eng. 23, 231–236.
Ryan, M.P. (Ed.), 1994. Magmatic Systems. Academic Press, San Diego, CA, p. 401.
Sammonds, P.R., Meredith, P.G., Main, I.G., 1992. The role of pore fluids in the generation of seismic precursors to shear fracture. Nature 359, 228–230.
Sammonds, P.R., Murrell, S.A.F., Rist, M.A., 1998. Fracture of multiyear ice. J. Geophys. Res. 102, 21795–21815.
Shapery, R.A., 1986. A micromechanical model for nonlinear viscoelastic behaviour of particle-reinforced rubber with distributed damage. Eng. Fract. Mech. 25, 845.
Shaw, H.R., 1980. The fracture mechanisms of magma transport from the mantle to the surface. In: Hargraves, R.B. (Ed.), Physics of Magmatic Processes. Princeton University Press, Princeton, pp. 201–264.
Schultz, R.A., 1993. Brittle strength of basaltic rock masses with application to Venus. J. Geophys. Res. 98, 10883–10895.
Schultz, R.A., 1995. Limits on strength and deformation properties of jointed basaltic rock masses. Rock Mech. Rock Eng. 28, 1–15.
Tullis, J., Yund, R.A., 1987. Transition from cataclastic flow to dislocation creep of feldspar. Geology 15, 606–609.
Tullis, T.E., Horowitz, F., Tullis, J., 1991. Flow laws of polyphase aggregates. J. Geophys. Res. 96, 8081–8096.
Weertman, J., 1968. Dislocation climb theory of steady-state creep. Trans. Am. Soc. Metals 61, 681–694.